Numerical Investigation of Flow Field Around a Ship
in Manoeuvring Motion

by   Osman Md. Amin*, *Student Member*   Kazuhiko Hasegawa*, *Member*

Summary

Viscous flow simulation of flow field around ships for manoeuvrability prediction has become a highly sought after issue now-a-days among the ship hydrodynamicists. As potential flow theory still lacks the versatility to consider the viscosity and flow separation effects in calculation, RANS simulation has gained its popularity in calculating detailed pressure and shear force distributions around drifting ships. The objective of this research work is to investigate the patter of flow around a manoeuvring tanker. An in-house code using unstructured grid based RANS solver has been developed to investigate the behavior of a ship in drifting motion. For unstructured grid the oscillations caused by the adoption of second order differencing scheme have been minimized through the implementation of a slope limiter algorithm in discretizing the diffusion term of the Navier-Stokes equation. A double hull model has been implemented in the manoeuvring simulation instead of considering the free surface flow. This approximation is justified when the ship speed is considered to be quite low (Fr<0.2) during drifting motion.

1. INTRODUCTION

RANS (Reynold's Averaged Navier Stokes) simulation has so far been effective from the perspective of providing a useful tool in understanding the flow phenomena around a manoeuvring ship. Although practical application of it in real time simulation is still far away from the reach of scientists, it's implication along with the EFD (Experimental Fluid Dynamics) data may provide a practical approach towards investigating the complicated flow field around the manoeuvimg ship. Concerning the accuracy for calculating the forces and moment acting on a manoeuvring ship, very few institutes have developed the efficient RANS codes. Among those the institutes like University of Iowa[1], MARIN[2], INSEAN[3], Mississippi State University[4] are in the forefront in carrying out manoeuvring simulation of ships. All these codes have their unique way of putting together the existing numerical methods for the solution of Navier-Stokes equations considering different turbulence models. Verification of the codes are done by mostly two different methodologies as proposed by Stern et al[5], Eca et al[6]. EFD data have been acquired for mostly four different ships which have been published in the web since SIMMAN workshop of 2008[7] was held and is available through personal contact with the workshop authorities. All these efforts have been put forth to verify existing methodologies available to predict manoeuvring behavior of ships.

The hull forces and moment constitute a large portion of the hydrodynamic forces that are acting on a ship in motion. Prediction of these forces and moment are crucial in understanding the behavior of ships in manoeuvring motion. In this context, Campana et al[8] tried to achieve a reduction in the computational time in simulating flow field around a ship hull using a multi-domain decomposition method, where the whole domain was divided into viscous inner region to be solved using finite difference scheme and an inviscid outer region which was solved by boundary integral element method. For two different stern shaped ship hulls, drifting in unbounded fluid, thorough analyses were conducted by Ohmori et al[9] to simulate the actual velocity and pressure distribution around the hull. Finite volume method along with subgrid scale turbulence model had been employed in this respect through the negligence of free surface effect. The velocity and pressure distributions at the aft perpendicular of both the ships show good agreement with the experiment data from qualitative point of view, where the mechanism of vorticity generation also has been investigated thoroughly. Toxopeus[10] extended similar kinds of analyses to find the hull hydrodynamic force and moment coefficients through the application of least square method on the RANS simulation results. The accuracy of different orders of Godunov type finite differencing schemes (Second order ENO scheme, third order upwind scheme and fourth order center scheme) have been verified[11] through flow simulation around a naval combatant hull. Three different control grid sizes (fine, medium, coarse) are incorporated in these analyses, where from the point of view of computational efficiency, the fourth order scheme resulted the slowest convergence when simulating unsteady flow. Usage of unstructured grid in RANS simulation has been a topic of debate for last couple of decades where application of large number of cells in the grid (around 9-10 Million) is considered to be reliable one in simulating the flow field, as has been addressed by Burg et al[4]. Similar conclusion were drawn by Fathi et al[12], suggesting inherent lack of predictability of forces and moment acting on a ship hull due to the usage of unstructured grid. These analyses inspired the authors to go for developing a RANS code on the basis of unstructured topology of the grid that comprises the space around a hull.

The hull-propeller-rudder interaction is largely depended upon the wake measurement in the propeller plane. None of

---

* Graduate School of Osaka University, Japan

the numerical simulations so far have been able to simulate accurately the wake distribution because of the empiricisms that are incorporated with the turbulence models. Flow simulation using different turbulence model for a particular hull has been conducted by Lungu et al[13] to provide some insights into this matter. Now-a-days DES (Detached Eddy Simulation) is becoming very popular in getting details of the vortex structures as shed by the drifting ships[14], although this kind of simulation incurs upon a large computational effort in predicting the flow field. Transient phases of turning manoeuvre are yet to be resolved by RANS simulation as being depicted by Atsavapranee et al[15] in his research, where turning diameter of the manoeuvring ship was predicted with quite reasonable accuracy.

In this paper, the objective of the Authors' is to develop a RANS based flow solver suitable to be applicable to any types of grids (structured/unstructured) and carry out the prediction of hull forces and moment acting on a drifting tanker, with nominal accuracy in calculating the wake behind the ship. For unstructured grid the oscillations in result caused by the adoption of second order differencing scheme have been minimized through the implementation of a slope limiter algorithm in discretizing the diffusion term of the RANS equation. The verification and validation of the code were achieved through the comparison of the simulated hull forces and moment acting on a tanker and a wigley hull with experiment data[16,17]. The simulated distribution of wake at the propeller plane suggests a lack in the generation of turbulent kinetic energy in the boundary layer, which can be attributed to the adoption of wall function in the prediction of velocity distribution near the wall. A double hull model has been implemented in the manoeuvring simulation instead of considering the free surface flow. This approximation is justified when the ship speed is considered to be quite low (Fr<0.2) during drifting motion.

2. NUMERICAL FORMUALTION OF COMPUTATIONAL METHOD

The governing equations for RANS simulation of incompressible flow around a body can be expressed by the following three equations, which as a group are called Reynolds Averaged Navier-Stokes equations:

Continuity equation:

$$\frac{\partial u_j}{\partial x_j} = 0 \qquad (1)$$

Momentum equation:

$$\rho \frac{\partial u_i}{\partial t} + \rho \frac{\partial}{\partial x_j}\left(u_i u_j\right) = -\frac{\partial p}{\partial x_i} + \frac{\partial}{\partial x_j}\left(\tau_{ij} - \overline{\rho u_i' u_j'}\right) \qquad (2)$$

where, stress tensor, $\tau_{ij} = \mu \left(\frac{\partial u_i}{\partial x_j} + \frac{\partial u_j}{\partial x_i} \right)$ (3)

In these equations, u_j represents the velocity components, x_j are the Cartesian coordinates, p is the pressure, μ is the dynamic viscosity and $\overline{\rho u_i' u_j'}$ is termed as the Reynolds

stress. The quantities without bar are considered to have mean values.

The closure of the Reynolds stress is achieved by considering it to be expressed as the following equation in the two equation k-ε turbulence model,

$$-\overline{\rho u_i' u_j'} = \mu_t \left(\frac{\partial u_i}{\partial x_j} + \frac{\partial u_j}{\partial x_i} \right) - \frac{2}{3}\rho \delta_{ij} k \qquad (4)$$

Here, k is the turbulent kinetic energy and μ_t is the eddy viscosity.

2.1 Solution for RANS Equation

Finite volume method for collocated arrangement of unstructured grid has been adopted in this analysis to discretize the convection and diffusion terms of the Reynolds Averaged Navier-Stokes equation. The whole domain has been discretized into a substantial number of control volumes (CV). For spatial discretization the steady state continuity and momentum equations are considered to be as,

$$\int_S \rho v \cdot n dS = 0 \qquad (5)$$

$$\int_S \rho v v \cdot n dS = \int_S \mu \, grad v \cdot n dS + \int_\Omega \rho b d\Omega \qquad (6)$$

These integral equations are applied to each CV and the integral quantities are evaluated at different points within the elemental volumes. The variable values are calculated at those points through linear interpolation of nodal values, except for the CV centers. No overlapping among the control volumes is assured through defining each cell face to belong to both cells to which it is common.

2.1.1 Discretization scheme

For satisfying the boundedness and second order accuracy in discretizing the convection term of Navier-Stokes equation, a modified NVD (Normalized variable diagram)[18] type differencing scheme, called gamma differencing scheme, has been utilized. In arbitrarily unstructured meshes (Fig.1) the difficulty in distinguishing the 'far upwind neighbor', which is a concept utilized in the application of the upwind scheme to find the directionality of the mesh, has rendered the application of TVD (total variation diminishing) schemes[19] unsatisfactory in terms of producing converged results. Gamma differencing scheme requires an intervention in the basic discretization practice to preserve the boundedness of the solution. This is basically achieved by blending central difference (CD) scheme along with the bounded upwind scheme (UD). The characteristics, like second order accuracy and the usage of compact computational molecule, made the CD scheme suitable for the application on arbitrary unstructured meshes.
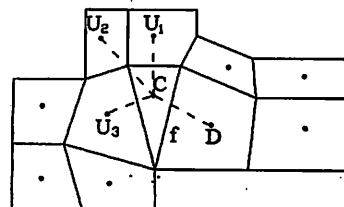

Fig. 1 Far upwind neighbors of an unstructured mesh

In order to overcome the inherent instability of NVD schemes, a blending factor γ has been implemented for
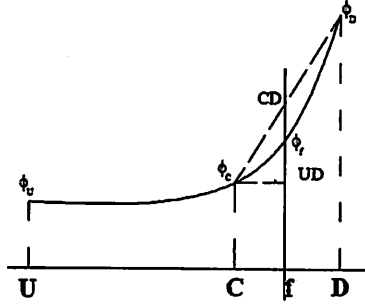

Fig. 2 Smooth transition for UD to CD in gamma differencing scheme

smooth transition between UD and CD, as can be seen from Fig.2. During transition from UD scheme to CD at cell centroid C, the value of normalized quantities (gradients) would remain constrained as,

$$0 < \tilde{\phi}_C < \beta_m \qquad (7)$$

where, β_m is a pre-specified constant of the differencing scheme, usually around 1/6. The blending factor γ has been defined on the basis of $\tilde{\phi}_C$ such that,

$$\text{If, } \tilde{\phi}_C = 0 \Rightarrow \gamma = 0 \text{, where, } \gamma = \tilde{\phi}_C / \beta_m$$

upwind differencing implemented   (8)

$$\text{else if, } \tilde{\phi}_C = \beta_m \Rightarrow \gamma = 1 \text{, where, } \gamma = \tilde{\phi}_C / \beta_m$$

central differencing implemented

Thus for unstructured grid, gamma differencing scheme can avoid the unphysical oscillations, that are common in other NVD type of difference schemes.

2.1.2 Limiters for second order solution reconstruction

The calculation of surface and volume integrals of Navier-Stokes equation for unstructured grid requires exact flux Jacobians to be computed at the faces of the control volumes. For second order differencing scheme the appearance of oscillations in solution process can be limited by the application of least square scheme as proposed by Barth et al[20]. This scheme consists of finding a weight factor for each control volume, which will limit the gradient for the linear algebraic equation solver. Barth's limiting function for the weight factor doesn't have the differentiability characteristics, which in turn adversely affects the convergence properties of the solver. Michalak et al[21] proposed that limiting value of the weight factor to be a cubic polynomial of the limiting function, which in turn solved the problem of the lack of differentiability of Barth et als' limiter in achieving a steady state solution. This limiter provides sufficient accuracy even in smooth regions without any local extrema. With these gradients known, the variables at different points within the control volumes have been calculated using bi-linear interpolation technique.

The second order approximations of surface and volume integrals of eqns. 5 and 6 render a set of non-linear algebraic equations, where the coefficient matrix appears to be a sparse matrix, as follows,

$$Q_p \phi_p + \sum_i Q_i \phi_i = B_p \qquad (9)$$

where, ϕ stands for $\phi = [u,v,w,p]^T$ and B_p stands for the discretized volume integrals of eqn.5 and 6. The suffix 'p' refers to a cell center under scrutiny and 'i' refers to the neighboring cell centers.

2.1.3 Pressure-momentum coupled solution

An implicit method, called PISO (pressure implicit with splitting operators) algorithm[22], is used to advance the momentum equation in time, where the discretized equations for the velocities at the new time step would be non-linear and of the form,

$$Q_P u_{i,P}^{n+1} + \sum_I Q_I^{u_i} u_{i,I}^{n+1} = B_{u_i}^{n+1} - \left(\frac{\delta p^{n+1}}{\delta x_i}\right)_P \qquad (10)$$

Due to the nonlinearity and coupling of the underlying integral equations, eqn.6 has been solved through outer iterations at each time step, in which the coefficient and source matrices are updated and then using inner iterations the linearized system of algebraic equations with fixed coefficients are solved. On each outer iteration the equations solved are,

$$Q_P u_{i,P}^{m^*} + \sum_I Q_I^{u_i} u_{i,I}^{m^*} = B_{u_i}^{n+1} - \left(\frac{\delta p^{n+1}}{\delta x_i}\right)_P \qquad (11)$$

Here, m* represents the intermediate values in each iteration. Eqn.11 at a node 'p' can be expressed as,

$$u_{i,P}^{m^*} = \tilde{u}_{i,P}^{m^*} - \frac{1}{B_P^{u_i}}\left(\frac{\delta p^{m-1}}{\delta x_i}\right)_P \qquad (12)$$

$$\text{Where, } \tilde{u}_{i,P}^{m^*} = \frac{B_{u_i}^{m-1} - \sum_I Q_I^{u_i} u_{i,I}}{Q_P} \qquad (13)$$

The modification of pressure field due to the enforcement of the continuity condition was achieved for intermediate iteration steps by the following Poisson equation,

$$\frac{\delta}{\delta x_i}\left[\frac{\rho}{Q_P^{u_i}}\left(\frac{\delta p^m}{\delta x_i}\right)\right]_P = \left[\frac{\delta\left(\rho \tilde{u}_i^{m^*}\right)}{\delta x_i}\right]_P \qquad (14)$$

After solving the Poisson equation for pressure, the final velocity field at the new iteration, u_i^m, has been calculated from the following equation for corrected velocities,

$$u_{i,P}^m = \tilde{u}_{i,P}^{m^*} - \frac{1}{Q_P^{u_i}}\left(\frac{\delta p^m}{\delta x_i}\right)_P \qquad (15)$$

The velocity field thus obtained although satisfies the continuity equation but does not satisfy the momentum equation. Therefore, another outer iteration is done and the process is continued until a velocity field which satisfies both the momentum and continuity equations is obtained.

For the solution of Poisson equation, a pressure correction is used instead of the actual pressure,

$$p^m = p^{m+1} + p' \qquad (16)$$

which renders the Poisson equation as,

$$\frac{\delta}{\delta x_i}\left[\frac{\rho}{Q_P}^{u_i}\left(\frac{\delta p'}{\delta x_i}\right)\right]_P = \left[\frac{\delta\left(\rho_{u_i}^{m*}\right)}{\delta x_i}\right]_P + \left[\frac{\delta\left(\rho\tilde{u}_i'\right)}{\delta x_i}\right]_P \qquad (17)$$

A further step of pressure correction did produce the PISO algorithm. The convergence is assumed to have been achieved when, $\left|p^{(m+1)} - p^{(m)}\right| < 10^{-4}$ (18)

2.1.4 Time discretization

A combination of two-time-level implicit Crank-Nicolson scheme and three-time-level explicit Richardson differencing scheme[23] has been adopted in this analysis. This scheme is more suitable than Crank-Nicolson schemes in a sense of producing less oscillatory solutions when the time steps are relatively small. The unsteady part of the momentum equation can be expressed as,

$$\left[\frac{\partial}{\partial t}\int_\Omega \rho u_i d\Omega\right]_P \approx \frac{\rho\Delta\Omega}{2\Delta t}\left(3u_i^{n+1} - 4u_i^n + u_i^{n-1}\right)$$
$$= Q_P{}'u_{i,P}{}^{n+1} - B_{u_i}{}' \qquad (19)$$

Where, $Q_P{}' = \frac{3\rho\Delta\Omega}{2\Delta t}$ and $B_{u_i}{}' = \frac{\rho\Delta\Omega}{2\Delta t}\left(4u_i^n - u_i^{n-1}\right)$

Eqn.19 transforms into the form of eqn.9, where unsteady parts are added at each sides of the equation to consider the time discretization in the analysis. Then using iterative solver for the system of nonlinear algebraic equations the solution at each time step is being obtained.

2.1.5 Solution of algebraic system of equations

An asymmetric version of the Bi-conjugate Gradient method has been used to solve the set of algebraic equations. Conjugate gradient method considers solving a nonlinear system of equations to be a problem of minimizing the nonlinear function with respect to several directions simultaneously, while searching in one direction at a time. Vorst et al[24] proposed a stabilized version of the method, which is adopted here in solving the algebraic system of equations. To improve the robustness of this iterative solver an ILUT preconditioning operation[25] has been carried out, where threshold drop tolerance has been kept to be 10^{-4}.

2.2 Turbulence Model

The turbulent flow model that has been used is based on the Reynolds Averaged Navier Stokes equations. Considering the flow parameters in turbulent flow to be composed of a time averaged value and a fluctuating component the continuity and momentum equation transforms into eqn.1 & 2 respectively, where the Reynolds stress term is expressed as eqn. 7. Among several popular models here in this analysis k-ε model with wall function formulation has been implemented[26]. From turbulent momentum equation (eq.2), combining with

continuity condition (eq.1), an equation for turbulent kinetic energy is determined empirically as,

$$\frac{\partial(\rho k)}{\partial t} + \frac{\partial\left(\rho\overline{u_j}k\right)}{\partial x_j} = \frac{\partial}{\partial x_j}\left(\mu\frac{\partial k}{\partial x_j}\right) - \frac{\partial}{\partial x_j}\left(\frac{\rho}{2}\overline{u_j{}'u_i{}'u_i{}'} + \overline{p'u_j{}'}\right) -$$
$$\overline{\rho u_i{}'u_j{}'}\frac{\partial\overline{u_i}}{\partial x_j} - \mu\overline{\frac{\partial u_i{}'}{\partial x_k}\frac{\partial u_i{}'}{\partial x_k}} \qquad (20)$$

Where, the term representing the turbulent diffusion of kinetic energy is modeled by use of a gradient diffusion assumption,

$$-\left(\frac{\rho}{2}\overline{u_j{}'u_i{}'u_i{}'} + \overline{p'u_j{}'}\right) \approx \frac{\mu_t}{\sigma_k}\frac{\partial k}{\partial x_j} \qquad (21)$$

The third term of the right hand side of eqn.20 represents the rate of production of turbulent kinetic energy by the mean flow, which is estimated as,

$$-\overline{\rho u_i{}'u_j{}'}\frac{\partial\overline{u_i}}{\partial x_j} \approx \mu_t\left(\frac{\partial\overline{u_i}}{\partial x_j} + \frac{\partial\overline{u_j}}{\partial x_i}\right)\frac{\partial\overline{u_i}}{\partial x_j} \qquad (22)$$

Determination of the length scale of the turbulence is modeled on the basis of observations that the rate of production and destruction of turbulence are in near balance, where energy dissipation, kinetic energy and length scale are related as,

$$\varepsilon \approx \frac{k^{3/2}}{L} \qquad (23)$$

For energy dissipation another equation can be formulated empirically as,

$$\frac{\partial(\rho\varepsilon)}{\partial t} + \frac{\partial\left(\rho u_j\varepsilon\right)}{\partial x_j} = C_{\varepsilon 1}P_k\frac{\varepsilon}{k} - \rho C_{\varepsilon 2}\frac{\varepsilon^2}{k} + \frac{\partial}{\partial x_j}\left(\frac{\mu_t}{\sigma_\varepsilon}\frac{\partial\varepsilon}{\partial x_j}\right) \qquad (24)$$

This model contains five parameters, the most commonly used values for them are:

$$C_\mu = 0.09; \quad C_{\varepsilon 1} = 1.44; \quad C_{\varepsilon 2} = 1.92; \quad \sigma_k = 1.0; \quad \sigma_\varepsilon = 1.3$$
$$\qquad (25)$$

To take account of the effect of viscous sub-layer of the boundary layer in calculation, the turbulent quantities near the wall have been calculated using the wall functions. Although the meshes near the wall were refined using prismatic cells, the distances of those cells from the wall weren't found to have similar distances. In some cases, the distance of the near wall cell sometimes exceeds the viscous sub-layer thickness and resides in the log-layer of the boundary layer. For this reason, at the wall, a two layer approach is used,

$$u^+ = y^+ \quad \text{if } y^+ < 11.067$$
$$u^+ = \frac{1}{\kappa}\ln y^+ + 5.25 \text{ if } y^+ > 11.067 \qquad (26)$$

where, $u^+ = \frac{u}{U_\tau}; \quad y^+ = \frac{yu_\tau}{\nu_w}; \quad U_\tau = \sqrt{\frac{\tau_w}{\rho_w}}$

The production of turbulent kinetic energy at the near wall cell is considered to be the average value between the viscous sub-layer edge, y_v and the log layer edge, y_n[26],

$$\bar{P}_k = \frac{\tau^2_{wall}}{\kappa C_{\mu}^{1/4} \rho k_p^{1/4} y_n} \ln(\frac{y_n}{y_v}) \quad (27)$$

where, τ_{wall} is the turbulent shear stress at the wall and k_p is the turbulent kinetic energy at the near wall cell.

The value of ε at the near wall cell, P, is considered to be,

$$\varepsilon_p = \frac{k_p^{3/2}}{C_l y_p} \quad (28)$$

where, y_p is the distance of the center of near wall cell.

Same differencing scheme is used to discretize both turbulent kinetic energy and energy dissipation equations

(eqn.20 & 24). The outer iterations of the momentum and pressure correction equations are performed using the value of eddy viscosity, which is based on the values of k and ε at the end of the preceding iteration. Then through another iteration the k and ε equations are made linear. After that again the eddy viscosity is calculated and another outer iteration is started.

2.3 Overall Algorithm of the flow solver

Being consistent with the above descriptions of the numerical methods, the total algorithm of the flow solver can be summarized by the following flow-chart:
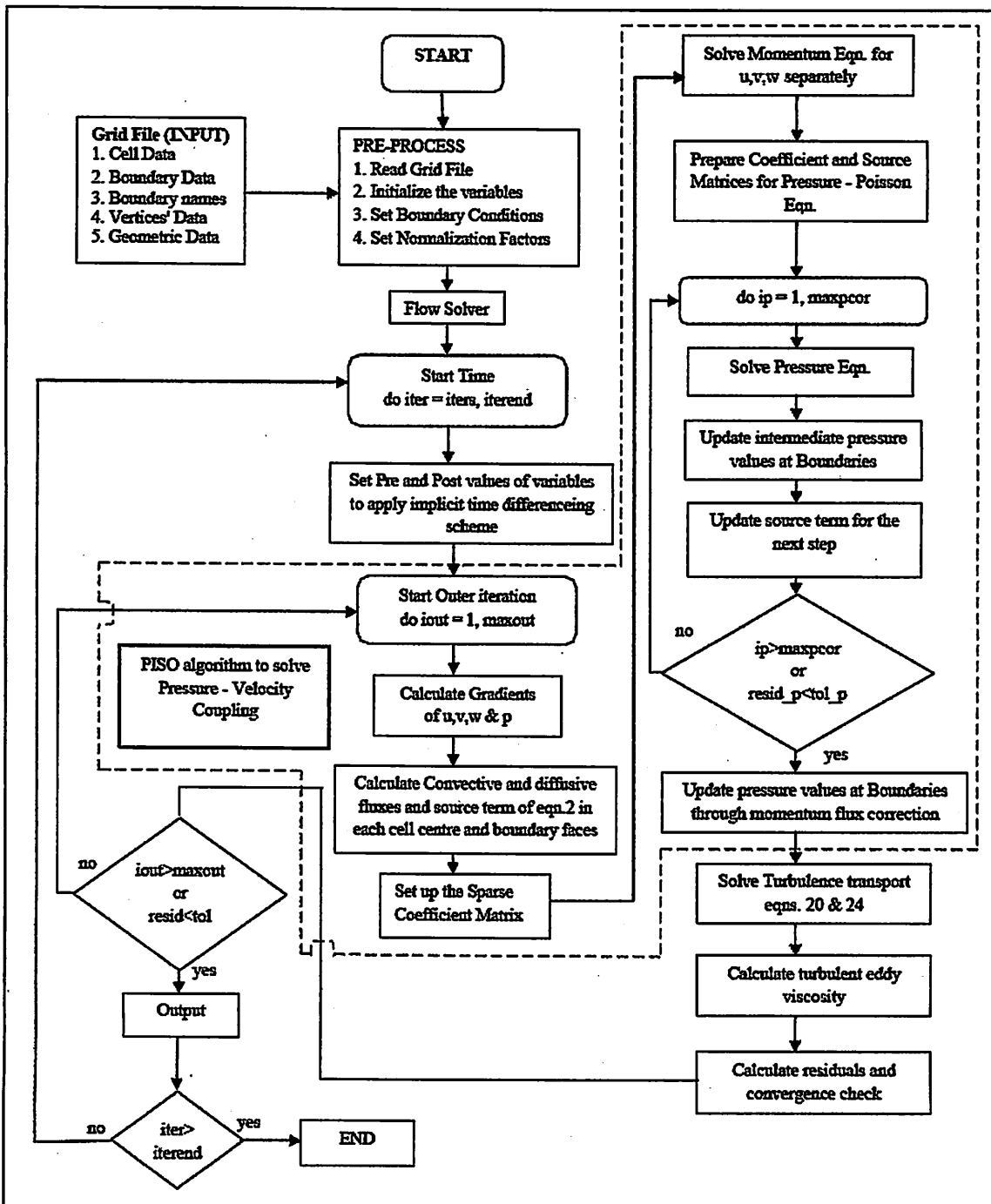
Fig 3 Flow-Chart for RANS Flow Solver

The terms 'maxout' and 'maxpcor' represent the iteration numbers used in the solution of pressure-velocity coupling (PISO algorithm) and pressure-poisson equation respectively. The dotted area in fig.3 represents the main part of the PISO algorithm.

3. SIMULATING CRITERIA FOR SUBJECT SHIPS

As a test case, the authors considered to simulate steady drifting motion of wigley hull and a tanker called KVLCC2M (Fig.4) in unbounded fluid for which the experimental data are available in publications[16,17]. For wigley hull only the straight ahead motion simulation has been conducted with three different grids to carry out the grid convergence study of the numerical result. The specifications of the models for which the data are available are given in Table 1.

a) Wigley hull

b) KVLCC2M hull
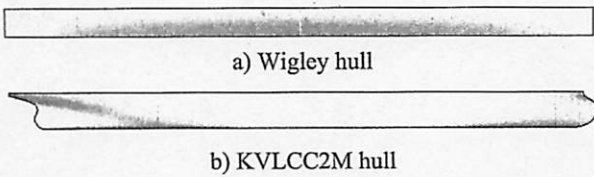
Fig. 4 hull shapes of two test ships

Table 1: Specifications of the ship and model

Principle Particulars				Wigley	KVLCC2M
Item	Symbol	Unit	Value		
Length between perpendiculars	Lpp	m	1.905		4.97
Breadth(molded)	B	m	0.238		0.9008
Draft(molded)	D	m	0.095		0.3231
Wetted surface area without appendages	S_w	m^2	0.511		6.5597
Centre of Buoyancy from midship (+forward)	l_{cb}	m	0.00		3.50
Block coefficient	C_B	-	0.4191		0.8098

3.1 Computational Domain and Grid Generation

The computational domain is taken to be of the shape of a basin, where the coordinate system is considered to be Cartesian in nature. The whole length of the domain for Wigley and KVLCC2M hulls are taken to be of 4.0Lpp and 3.0Lpp in size (Fig.5b & 5a) respectively, where the breadth and depth of the domains are considered to be of 6.0 times the breadth and 8.0 times the draft of both ships respectively. The grid topology is taken to be unstructured in nature. ICEM CFD part of ANSYS software has been used to generate the grids. Octree algorithm has been used to generate unstructured grids for the whole domain. The grids near the surface of the hull have been discretized into 3D prism cells to make the normal of the grid faces perpendicular to the surface (Fig.6).
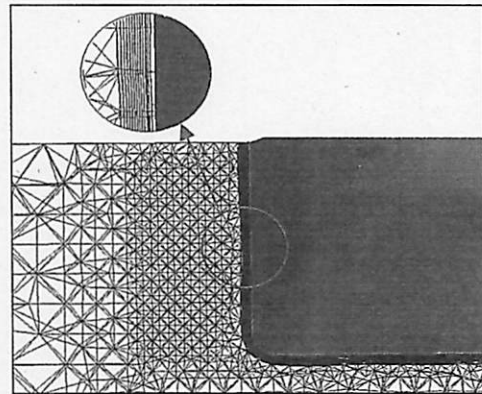

Fig. 6 Prismatic cell distribution near the hull in unstructured grid.

3.2 Boundary Conditions

To implement the no-slip condition on the impermeable wall, the normal viscous forces are considered to be zero. The shear stress is calculated in case of finite volume method through the use of velocity gradients parallel to the wall. For k-ε model all the turbulence quantities except, the energy dissipation term, ε are considered zero at the wall. On the basis of the 'law of the wall' a wall function approach in the determination of energy dissipation near the wall has been utilized, where dissipation and turbulence production terms in the turbulence model have specific expression to be calculated at the first grid near the wall[24].
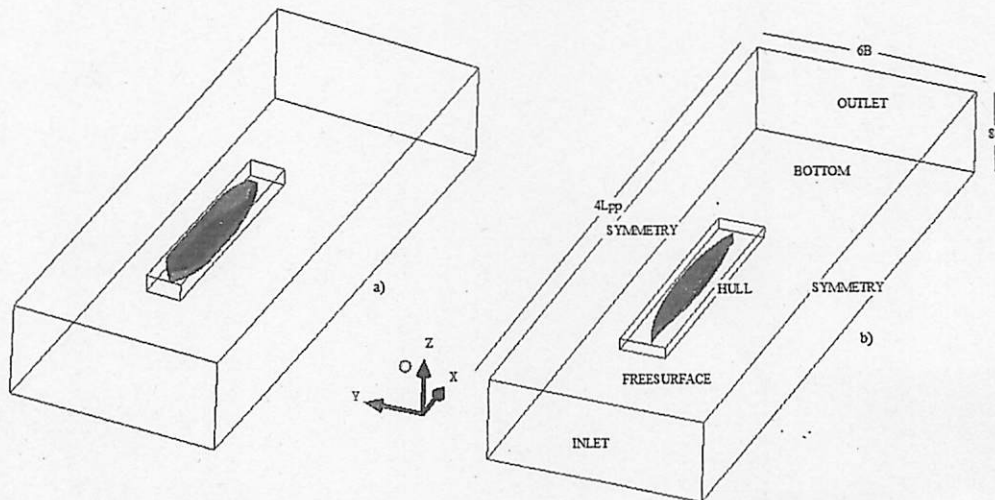

Fig.5 a) KVLCC2M hull domain, b) Wigley hull domain with boundary surfaces

Symmetry conditions are applied to the side walls, where the shear stress is considered to be zero while the normal stress is not. The normal stress is calculated from the velocity gradient normal to the plane. At the inlet the velocity components correspond to the Reynolds number used during the experiments. At downstream of the ship the flow is calculated through second order linear extrapolation along the grid lines from the interior to the outlet. The bottom is considered to have no vertical component of velocity. The free surface modeling hasn't been considered in our simulation. So, instead of the free surface boundary condition a mirror image has been applied. In this case the velocity gradients normal to the surface has been termed as zero along with the normal velocity.

4. RESULTS

4.1 Verification and Validation Study

The verification and validation study of the code has been carried out on the basis of the V&V methodology proposed by stern et al[27]. At first, the study has been done on the Wigley hull running in straight ahead motion at a Reynolds number of 2.098×10^6. Three different grids (coarse, medium and fine) are being used (Table 3) to validate the total resistance coefficient, C_T. The simulated frictional resistance coefficient, C_F has been compared to the ITTC57 model ship correlation line formulae. The experiment data for this case has been collected from results published by Millward et al[17]. Table 2 shows the validation data of C_T, C_F & pressure coefficient C_P in straight ahead motion of wigley hull. The term ε represents the difference in percentage between successive grid results. Time history of C_T for three different grids are shown in Fig.7.

only composed of experimental, U_D and grid, U_G uncertainty,

$$U_V = \sqrt{\left(U_D^2 + U_G^2\right)} \qquad (30)$$

Since C_F & C_P both shows oscillatory convergence ($R_G<0$, $|R_G|<1$) only for C_T the grid convergence study has been carried out. The reason is that, Richardson extrapolation is largely dependent upon the first term of the Taylor series expansion of the discretization error, which may not be true when oscillatory convergence occurs. Further study later would be carried out to statistically solve the extrapolation of this oscillatory convergence. In order to calculate the order of accuracy for the verification purposes, we have used the value of 2 as the estimated order of accuracy. As can be seen from Table 2 that refinement of the grid did improve the value of C_P to a slight extent as compared to the friction coefficient C_F. The comparatively larger difference between experimental and simulation data for C_P probably is due to the negligence of free surface effect in the calculation at a Froude number of 0.253. Since the value of experimental data uncertainty is not available from the collected data, we assumed it to have a value of 4%. Using this value, the validation is not achieved as can be seen from the Table 2, where the comparison error, $E = D - S$, has been found out to be slightly higher than the validation uncertainty, U_V (Table 2). As we haven't been able to use the same grid refinement ratio for those three grids, because of the inherent problems related to the unstructured grid generation, the validation uncertainty may have gotten influenced by this factor. On the contrary, if the value of Uv is considered to be around 5% the validation is achieved, which ·

Table 2. Verification and Validation of C_T (*10^{-3}), C_P(*10^{-3}) and C_F(*10^{-3}) for Wigley hull at beta 0^0

	Coarse	Medium	Fine	Convergence ratio, R_G	Order of accuracy, P_G	Correction factor for Uncertainty C_G	U_{SN} (%)	U_V (%)	Exp. data, D	Comparison Error, E
No. of cells	868299 S_3	1282518 S_2	1478944 S_1							
C_T	4.98	5.015	5.02	0.14	13.65	18.16	0.586	4.0427	5.232	4.223% of S_1
ε		0.702%	0.1%							
C_P	0.87	0.847	0.88	-1.43	-	-	-	-	1.212	
ε		-3.75%	3.89%							
C_F	4.1	4.16	4.138	-0.36	-	-	-	-	4.02 (ITTC)	
ε		1.46%	-0.53%							

Richardson extrapolation method is the basis of this particular validation method, where validation uncertainty is being defined to be,

$$U_V = \sqrt{\left(U_D^2 + U_I^2 + U_G^2 + U_T^2 + U_P^2\right)} \qquad (29)$$

Since, we used implicit time differencing scheme, we have considered the time step related uncertainty to be negligible. Therefore, we have considered the validation uncertainty to be

has been considered in the analyses carried out by Sakamoto et al[28].

Also the total resistance coefficient, C_T, of KVLCC2M running in straight ahead motion has been verified and validated using the same method. Grid Convergence study was carried out for three different grid sizes (coarse, medium and fine) as can be seen from table 3. The time histories of the total resistance coefficient for those three cases are plotted in Fig. 8.
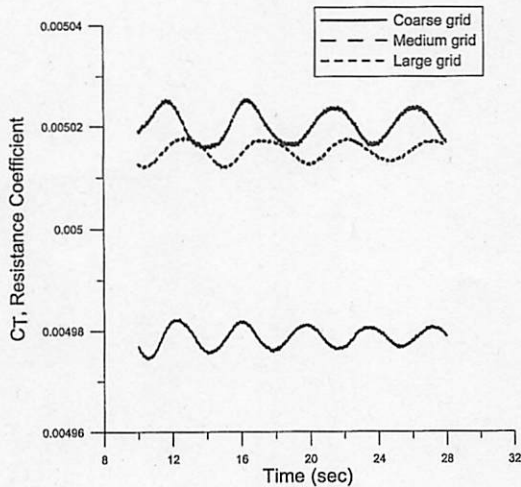
Fig. 7 Time history of C_T at beta 0^0 for three different grids of Wigley hull

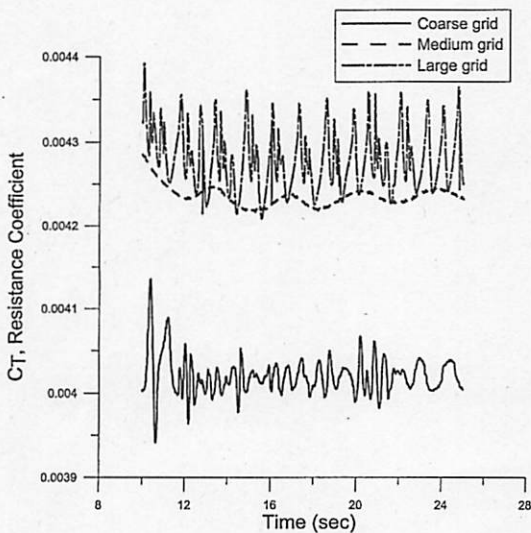Fig. 8 Time history of C_T at beta 0^0 for three different grids of KVLCC2M hull.

As can be seen from Fig.8 that, as the grid gets finer the values are getting much closer to the experimental value. Finer grid is showing larger oscillations due to the fact that for fine grid the second order differencing scheme is much active rather than the upwind scheme.

Table 3 Grid Convergence study for Total Coefficient of Resistance, C_T (*10^{-3}) for KVLCC2M at beta 0^0

Grid	Coarse	Medium	fine	Exp. Data
No. of cells	862737	1906720	2445654	
C_T(*10^{-3})	4.019	4.234	4.278	4.37
Difference(% of previous grid value)		5.35%	1.028%	

Table 4 Validation of Uncorrected total Resistance for KVLCC2M at beta 0^0

Comparison Error, E (% of value exp. data)	U_V	U_D	U_{SN}
2.15%	4.4076%	3.3%	2.92%

In this context, we find the Comparison error, $E = D - S$, to be less than the validation uncertainty (Table 4), which validates the study for the total resistance coefficient of KVLCC2M tanker in straight ahead motion. That means although we have considered double body image model instead of undulating free surface, for this low speed case the modeling error is quite negligible.

4.2 Drifting Cases

Several drifting cases for KVLCC2M hull have been simulated to validate the predictability of the developed code. Because of the usage of the unstructured grid the number of grid elements varied from case to case. The lowest and highest numbers of grid elements used were of around 900K and 1.7M cells respectively, which comprised of tetrahedral, prismatic and hexahedral elements. Because of the complicated nature of the unstructured grid topology, the number of cells in each grid got varied during its generation. Therefore, the number of cells in the grids basically depends upon the geometric domain and the desired concentration of cells near the hull for each of the cases. This may give rise to the ambiguity related to the grid dependency of the code. But the verification and validation study done in section 4.1 provides the evidence of robustness of the code in terms of producing low grid uncertainty in the result. The non-dimensional drag ($C_x = F_x / (0.5\rho U^2 L_{pp} d)$), lateral force ($C_y = F_y / (0.5\rho U^2 L_{pp} d)$) and yaw moment ($C_N = M_z / (0.5\rho U^2 L_{pp} d)$) coefficients for different drifting cases are being compared in Fig.9, 10 &11, where in an average the calculated and experimental data shows around 7-8% difference in values. The simulating conditions for different drifting cases are given in Table 5, where y+ (non-dimensional distance from the solid surface) is obtained from simulated data.

Table 5. Simulating conditions for different test cases

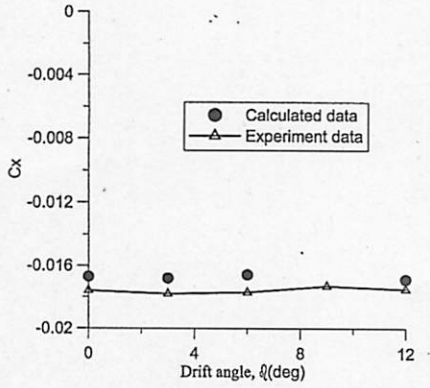| Drift angle, $(^0)$	Reynolds No.	Grid Size	
		Mesh Size(elements)	Y+(min/max)
0	4.011e6	862737	5/54
3	3.945e6	967467	8/58
6	3.967e6	1467409	10/60
12	4.00e6	1677043	7/67

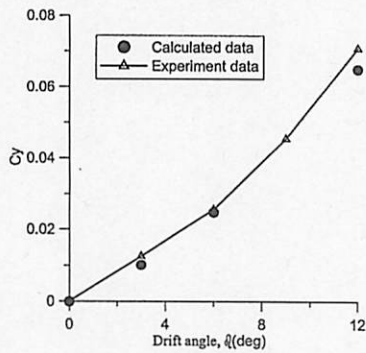Fig. 9 Drag coefficient, C_x vs drift angle, $\beta(^0)$

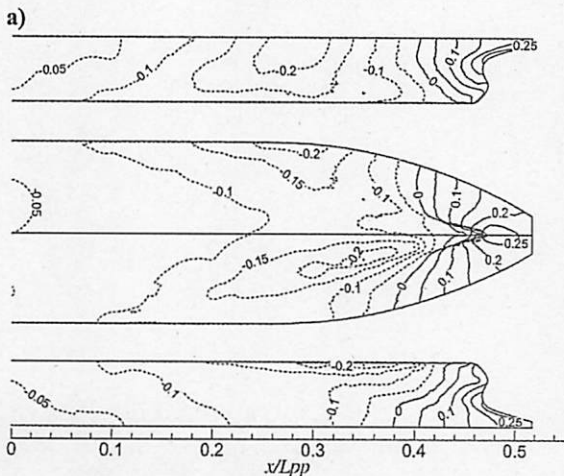Fig. 11 Yaw moment coefficient, C_N vs drift angle, $\beta(^0)$

Fig. 10 Lateral force coefficient, C_Y vs drift angle, $\beta(^0)$

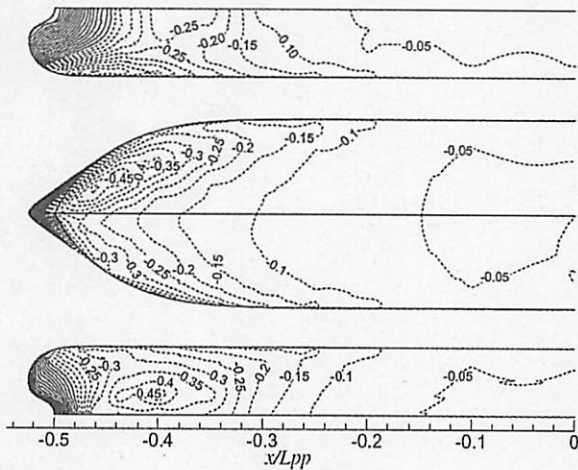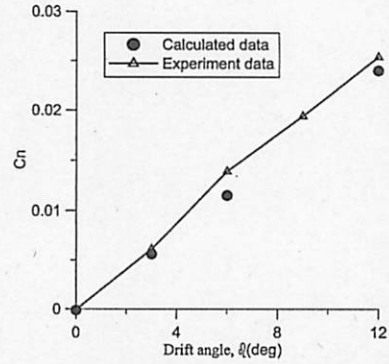The pressure contours ($C_p = P/(0.5\rho U^2)$ for one case ($\beta = 6^0$) has been plotted with an interval of 0.05, where Fig.12 & 13 depict the experimental and calculated pressure distributions along the length of the hull respectively. Comparison between the two distributions shows that qualitatively and quantitatively the pattern of pressure contours resemble to each other reasonably well. However, at the aft part the calculated pressure contours show a relatively significant difference in the negative pressure generation compared to the experimental data. This tendency may have occurred due to the near wall approximation of the turbulent
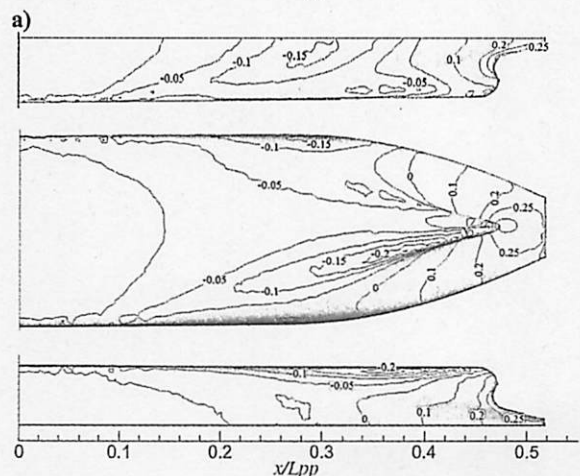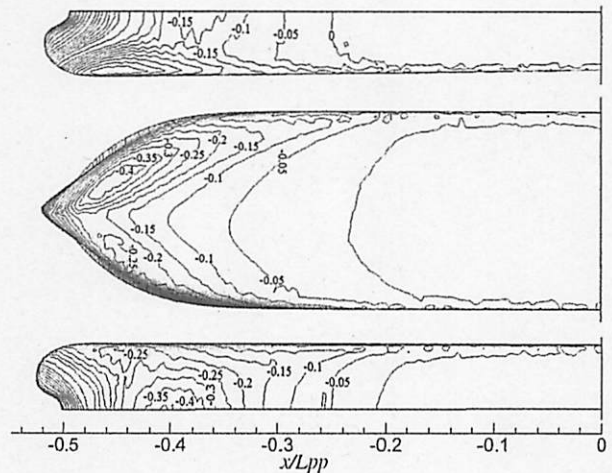

a)

b)

Fig. 12 Experimental data on distribution of surface pressure coefficient for $\beta = 6^0$ (a: fore & b: aft)

a)

b)

Fig. 13 Computed distribution of surface pressure coefficient for $\beta = 6^0$ (a: fore & b: aft)

energy dissipation rate (eqn.28). The production term of turbulent kinetic energy (eqn.27) also didn't consider the pressure gradient near the wall which may have large influence in the results for highly vortical flows. The imbalance in the production and dissipation of turbulent kinetic energy may produce the difference in the distribution of pressure contours at the stern. The pattern of the pressure contours although seem to be well captured in the simulation.

The axial velocity distribution at the propeller wake for two different drifting angles are shown in Fig.14 & 15. The simulated velocity field at the propeller plane although manifests an ability to qualitatively capture the distribution of flow around the ship wake, the development of vortices at the

a)

b)

Fig. 14 Axial Velocity Field contours in propeller plane for

$\beta = 6^0$ (experiment: a, simulated: b)

a)

b)

Fig. 15 Axial Velocity Field contours in propeller plane for

$\beta = 12^0$ (experiment: a, simulated: b)

wake haven't gotten properly simulated as can be seen through the comparison with experimental data. As wall function model for velocity distribution has a lack in generating proper shear force distribution along the hull, we can see the simulated values for sway force and yaw moment coefficients (Fig. 10 & 11) are having larger discrepancies as the drifting angles become larger. Also the empiricism involved with the turbulence model have large bearing in the simulation of proper wake distribution. Although the shed vortices far from the boundary layer at each drifting cases are not simulated properly, the velocity distribution at the propeller plane seems to be much better simulated than other places.

5. CONCLUSIONS

The establishment of the RANS solver for the prediction of manoeuvrability of drifting ships is the first step towards the development of a robust numerical method for simulating the ship behavior in sea for various surrounding conditions. In this respect, the conclusions which can be arrived at on the basis of these analyses are as follows:

1) An in-house code for RANS simulation has been established to simulate the flow field around a ship in drifting motion.

2) The estimation of forces and moment acting on the ship under steady drift motion shows reasonable approximation in calculating the experimental data.

3) Adoption of unstructured grid didn't put that much constraint in calculating approximately the forces and moment acting on the ship hull, although overall prediction of the flow field, especially at the wake, needs lot more detail analysis, which are under investigation at this moment.

4) The empiricism involved with the turbulence models, especially the usage of wall function, prescribe a thorough investigation on the application of different turbulence models to verify the wake at the propeller plane for better prediction of manoeuvrability of ships.

6. REFERENCES

1) Paterson, E.G., Wilson, R.V., and Stern, F.: General-purpose parallel unsteady RANS ship hydrodynamics code: CFDSHIP-IOWA, The University of Iowa, Iowa Institute of Hydraulic Research, IIHR Report No 432, 2003.

2) M. Hoekstra and L. Eca,: PARNASSOS: an efficient method for ship stern flow calculation, Third Osaka Colloquium on Advanced CFD Applications to Ship Flow and Hull Form Design, Osaka, Japan, pp.331-357.

3) Mascio, A.D., Broglia, R., and Muscari, R.: On the application of the single-phase level set method to naval hydrodynamic flows, Computers and Fluids, 2007, Vol.2, pp.868-886.

4) Burg, C.O.E., Sreenivas, K., Hyams, D.G. and Mitchell, B.: Unstructured nonlinear free surface simulations for the fully appended DTMB model 5415 series hull including rotating propulsors, 24th Symposium on Naval Hydrodynamics, Fukuoka, Japan, 2002, pp.192-210.

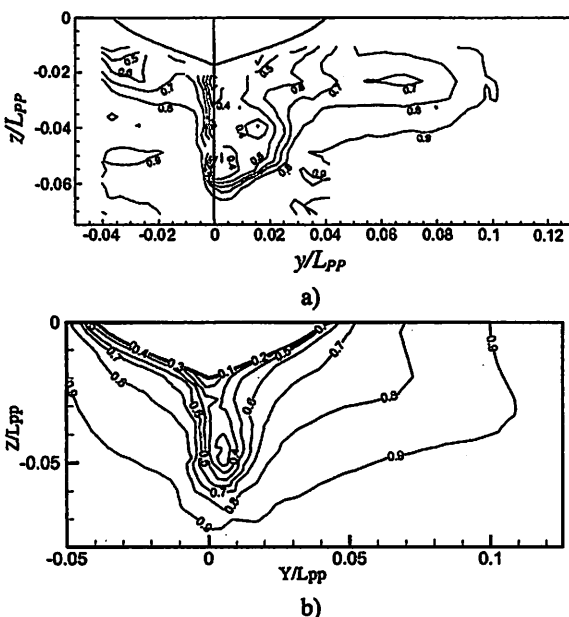5) Stern, F., Wilson, R.V., Coleman, H.W., Paterson, E.G.: Comprehensive approach to verification and validation of
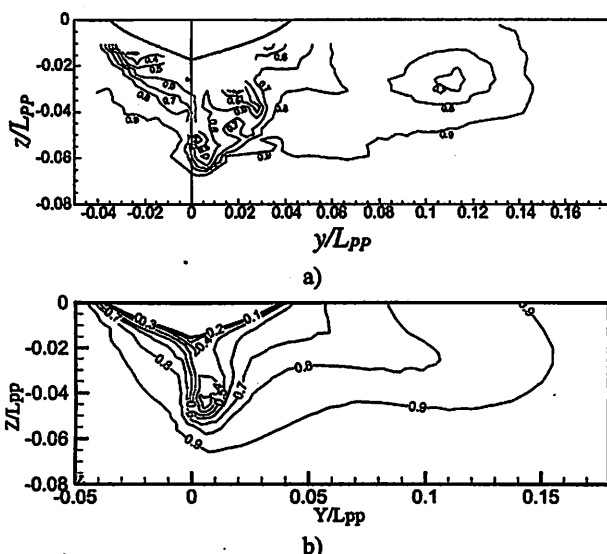
CFD simulations – part 1: methodology and procedures, Journal of Fluids Engineering, Vol. 123, pp.793-802.

6) L. Eca and M. Hoekstra: An evaluation of verification procedures for CFD applications, 24th Symposium on Naval Hydrodynamics, Fukuoka, Japan, 2002, pp.568-587.

7) Website – "www.simman2008.dk/".

8) Campana E., Mascio, A.D., Esposito, P.G., and Lalli, F.: Viscous-inviscid coupling in free. surface ship flows, International Journal for Numerical Methods in Fluids, Vol.21, 1995, pp.699-722.

9) Ohmori, T., Fujino, M., and Miyata, H.: A study on flow field around full ship forms in maneuvering motion, Journal of Marine Science and Technology, Vol.3, 1998, pp.22-29.

10) S. L. Toxopeus: Deriving mathematical manoeuvring models for bare ship hulls using viscous flow calculations, Journal of Marine Science and Technology, Vol.14, 2009, pp.30-38.

11) Mascio A. D., Broglia, R., and Muscari, R.: Prediction of hydrodynamic coefficients of ship hulls by high-order Godunov type methods, journal of Marine Science and Technology, Vo.14, No.1, 2009, pp.19-29.

12) Fathi, F., Kaij, C., and Koop, A.: Predicting loads on a large carrier with CFD, Proceedings of the 29th International Conference on Ocean, Offshore and Arctic Engineering, Shanghai, China, 2010.

13) A. Lungu and F. Pacuraru: Free surface flow around an appended hull, 25th IAHR symposium on Hydraulic Machinery and Systems, 2010.

14) Heredero, A.P., Xing, T. and Stern, F.: URANS and DES analysis for a Wigley hull at extreme drift angles, Journal of Marine Science and Technology, Vol.15, 2010, pp.295-315.

15) Atsavapranee, P., Miller, R., Dai, C., Klamo, J., and Fry, D.: Steady-turning experiments and RANS simulations on a surface combatant hull form (model #5617), 28th Symposium on Naval Hydrodynamics, Pasadena, 2010, pp.12-17.

16) K. Kume, K., Hasegawa, J., Tsukada, Y., Fujisawa, J., Fukasawa, R., and Hinatsu, M.: Measurements of hydrodynamic forces, surface pressure, and wake for obliquely towed tanker model and uncertainty analysis for CFD validation, Journal of Marine Science and Technology, 2006, Vol.11, pp.65-75.

17) Millward, A. and Bevan, M.G.: Effect of shallow water on a mathematical hull at high subcritical and supercritical speeds, Journal of Ship Research, Vol.30, No.2, pp.85-93, 1986.

18) Jasak, H., Weller, H.G. and Gossman, A.D.: High resolution NVD differencing scheme for arbitrarily unstructured meshes, International Journal of Numerical Methods in Fluids, Vol.31, 1999, pp.431-449.

19) P.K. Sweby: High resolution schemes using flux limiters for hyperbolic conservation laws, SIAM Journal of Numerical Analysis, Vol.21, 1984, pp.995-1011.

20) Barth, T.J., and Jespersen, D.C.: The design and application of upwind schemes on unstructured meshes, AIAA paper 89-0366, 1989.

21) Michalak, K. and Gooch, C.O.: Limiters for unstructured high-order accurate solutions of the Euler equations, AIAA, 46th Aerospace Sciences Meeting, 2008.

22) Issa, R.I. : Solution of implicitly discretized fluid flow equations by operator-splitting, Journal of computational physics, Vol.62, 1986, pp.40-65.

23) Shvedov, A.S.: A three-time-level explicit difference scheme of the second order of accuracy for parabolic equations, Mathematical Notes, Vol.60, No.5, 1996, pp.562-568.

24) Vorst, V.D. and Sonneveld, P.: CGSTAB, a more smoothly converging variant of CGS, Technological Report 90-50, Delft University of Technology.

25) Chapman, A., Saad, Y., and Wington, L.: High order ILU preconditioners for CFD problems, International Journal for numerical methods in fluids, vol.33, pp. 767-788, 2000.

26) Craft, T.J., Gerasimov, A.V., Iacovides, H., and Launder, B.E.: Progress in the generalization of wall-function treatments, International Journal of Heat and Fluid Flow, 2002, Vol.23, pp.148-160.

27) Stern, F., Wilson, R., and Shao, J.: Quantitative V&V of CFD simulations and certification of CFD codes, International Journal for Numerical Methods in Fluids, 2006, Vol.50, pp.1335-1355.

28) Sakamoto, N., Wilson, R.V., and Stern, F.: Reynolds Averaged Navier-Stokes simulations for high-speed wigley hull in deep and shallow water, Journal of Ship Research, Vol.51, No.3, pp.187-203, 2007.